Virtual Special Issue
Ocean Surface Waves

Comparing wavelengths simulated by the coastal wave model CWAM and TerraSAR-X satellite data

Claus Gebhardt [a],[*], Andrey Pleskachevsky [a], Wolfgang Rosenthal [a], Susanne Lehner [a], Peter Hoffmann [b], Jens Kieser [b], Thomas Bruns [b]

[a] *German Aerospace Center, Remote Sensing Technology Institute, Maritime Security Lab, Bremen, Germany*
[b] *German Meteorological Service, Referat WV 13 - Seeschifffahrtsberatung, Hamburg, Germany*

A B S T R A C T

The accuracy of the high resolution coastal wave forecast model CWAM is validated on the basis of sea state information from satellite images of TerraSAR-X (TS-X). At the same time, the performance of the satellite retrieval of sea state parameters is demonstrated. Employing 2-dimensional spatial Fourier Transformation, image spectra are derived from TS-X and locally varying patterns of the peak wavelength are provided using state-of-the-art satellite retrieval. Subsequently, wavelength comparisons are performed between a typical set of TS-X scenes acquired in December 2013 over the German Bight and the model hindcasts. The results are mostly in reasonable agreement. Potential shortcomings of the wave model are discussed as well.

1. Introduction

Monitoring the sea state from space, including spectral quantities like the wavelength and travel direction, has started in 1978 with the synthetic aperture radar (SAR) on SeaSat (Beal et al., 1983). Improvements were achieved with the ESA satellites ERS-1, ERS-2, and ENVISAT, operating in C-band (Li et al., 2008; 2011, and references therein). A recent historical overview on the SAR wave-mode being operated on these three satellites, and the use of the wave-mode data at ECMWF to improve numerical wave predictions, is given in (Hasselmann et al., 2012). The resolution of the SAR wave-mode of ENVISAT and the ERS-satellites was sufficient for measuring long waves (about 100 m and longer) and for the comparison to buoys for respective frequencies (0.12 Hz and shorter). The satellite data were useful for deep water areas (the dispersion relation for deep water waves was important for the comparison of wave number and frequency spectra). For deep water conditions, the derivation of the significant wave height (SWH) from C-band satellites, independent from wave model input, is possible by empirical algorithms (e.g. Schulz-Stellenfleth et al., 2007). Beside Radarsat, also operating in C-band since 2007, data are provided as well from high resolution

SAR-satellites operating in X-band like TerraSAR-X and COSMO-Skymed. At present, several high resolution radars are in space that permit spatial resolution down to 1 m and less. We use in the following the Stripmap mode of the TerraSAR-X satellite (TS-X) which has a resolution of around 3 m.

A comprehensive description of the near-real time retrieval of sea state parameters and wind conditions from TS-X is given in Lehner et al. (2014). In addition to these near-real time services, there are follow-on applications such as the retrieval of the water depth from the wavelength observed by TS-X (Pleskachevsky et al., 2011). The capability of measuring the SWH in the deep water as well as in the coastal environment by X-band SAR has been shown in Bruck and Lehner (2012). They used an empirical algorithm and made comparisons to in-situ data from buoys. A bias of 10% with respect to the buoy data was observed. In addition, peak wavelengths and directions from image spectra of TerraSAR-X and Tandem-X were compared to deep water wave measurements. These quantities were derived by a direct approach, i.e. without using inversion techniques.

The forecast quality of numerical wave models may be evaluated by comparing model hindcasts with TS-X data. In this article, we focus on peak wavelength measurements by high resolution SAR acquired over a coastal environment and compare the data with the results of a high resolution wave model of the German Meteorological Service (Deutscher Wetterdienst, DWD). The comparison is non-trivial because the model uses frequency-direction coordinates and

* Corresponding author. Tel.: +49 421 244201862.
E-mail address: Claus.Gebhardt@dlr.de (C. Gebhardt).

the SAR measures Cartesian components of the peak wavenumber vector. The peak values of sea state spectra may differ in these two coordinate systems. The dispersion relation between wave frequency and wavenumber depends on tidal water level and current influences which are space and time dependent. The wave model receives the actual current and water level changes by employing a one way coupling with an ocean model. The outcome of the comparison provides valuable indications on the ability of the model to accurately predict the wavelength. The latter is vital to the forecast quality of the model as the group speed of waves is in general wavelength dependent.

Previously, comparisons between TS-X and both model data from the wave model WAM and buoy data were made in Bruck and Lehner (2013). In this paper, a case study was conducted for TS-X scenes inside the German Bight which represent different sea state conditions. The sea state data from these scenes were sufficiently validated and interpreted using WAM hindcast data.

Meanwhile, a modification of WAM, called CWAM, is run preoperationally at the DWD. A first comparison of the SWH from TS-X with the respective CWAM model data was shown in Kieser et al. (2013). For a statistical ensemble of TS-X images, the SWH was compared to CWAM in the recent article of Pleskachevsky et al. (2015). The aim was both a validation of the wave model and a refinement of the algorithm retrieving the SWH from satellite. This included as well a validation of CWAM against buoy measurements. The overall statistics showed that the wave model has a tendency to overestimate the SWH with respect to TS-X data. The timing of the wind input of the model was considered to be one source of modelling error. In our article, deriving the peak wavelength from TS-X is the focus. CWAM is validated by wavelength comparisons between TS-X scenes acquired over the German Bight and wave model hindcasts. The approach followed here is based on conducting case studies for selected satellite images. This results in reasonable agreement between satellite and model as well as a certain degree of disagreement which shows some basic shortcomings of the model and/or its input parameters. Typical modelling errors include an underestimation of the model peak wave period, the relative weighting of different spectral peaks, and the wind input of the model.

The paper is structured as follows. In Section 2, the sea state (and wind) analysis of TS-X satellite images and the numerical wave model CWAM are described. The preparation of data for the following comparisons is explained. Section 3 is the results part. First, statistical parameters such as the bias, root-mean-square-difference, correlation, and scatter index are introduced for subsequent use. Second, example plots on the comparisons of the peak wavelength between satellite and model are presented. Third, the statistics of all comparisons of the peak wavelength is condensed into one table. Fourth, the results are discussed. This involves diagnosing potential sources of error with plausibility checks being performed. An overall summary of this study is given in Section 4.

2. TS-X and CWAM data

2.1. The TS-X satellite

2.1.1. Instrumentation

TS-X was launched in June 2007 and started routine operation in January 2008. It hosts a state-of-the-art X-band synthetic aperture radar operating at a wavelength of 3.1 cm. TS-X achieves high spatial resolution and has a recurrence time of 11 days. The same geolocation may be overpassed in different geometry in shorter time. TS-X observations are independent of sun light and cloud conditions. The relatively low orbit (∼500 km altitude) of the TS-X platform is advantageous against non-linear imaging effects of ocean waves. For more details on TS-X see Breit et al. (2010).

TS-X operates in 3 basic imaging modes such as the ScanSAR, Stripmap, and Spotlight mode. With the antenna beam held fixed
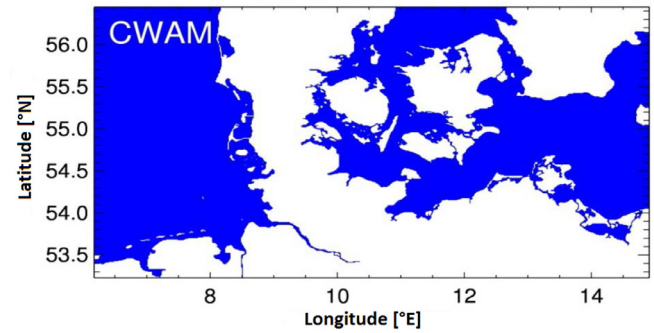

Fig. 1. The CWAM model input and output cover the area of 6.1736°E and 14.9097°E and 53.2292°N to 56.4458°N. This comprises the German Bight and western part of the Baltic Sea.
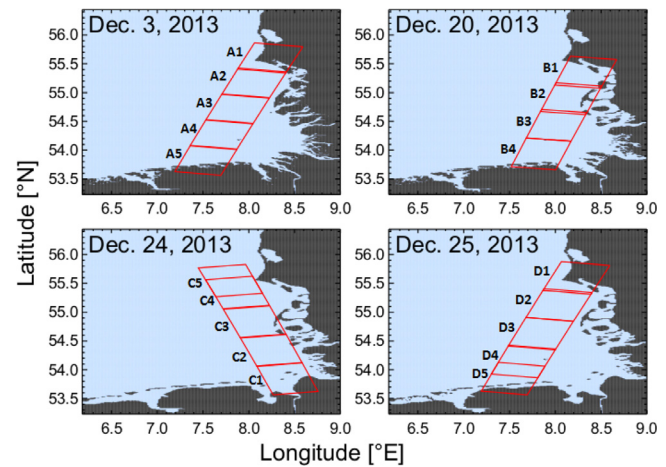

Fig. 2. The German Bight area is shown for the dates of December 3, 6 UTC, December 20, 6 UTC, December 24, 17 UTC, and December 25, 6 UTC. The boundary between land and water is based on the CWAM model. Water/land is coloured blue/black. On each day, the position of the TS-X images are highlighted by red boxes. From top to bottom, these are the images A1–A5 on December 3, B1–B4 on December 20, and D1–D5 on December 25 and from bottom to top, the images C1–C5 on December 24. Denoting the images by A1 to D5 is in accordance with Table 1. In the following figures, CWAM input and output data are shown for the same dates and area.

in Stripmap mode, the swath width is 30 km. Stripmap images are typically provided comprising an area of 30 × 50 km. The acquisition length in Stripmap mode may be extended up to 1650 km (at 30 km width). Thus, scenes comprising several images are acquired. In this study, only Stripmap scenes of MGD (=Multi Look Ground Range Detected) type are used. Their length is 4–5 images. All of them were acquired in VV polarisation. They have an equidistant pixel spacing of 1.25 m both in azimuth and range direction (i.e. the flight and cross-flight direction of the satellite). As a result of the multilooking technique, MGD products have effectively reduced speckle noise. More information on TS-X products can be found at http://www.dlr.de/TerraSAR-X.

2.1.2. Data on the peak wavelength and direction

The sea state retrieval achieves high spatial resolution by analysing subscenes of the full TS-X image. For each subscene, the image power spectrum is determined by 2-dimensional Fast Fourier transformation (FFT). The peak wavelength and direction directly follow from the image power spectra. This relationship was shown by Bruck and Lehner (2012) by validating TS-X against collocated buoy measurements. Note that the scatter index between TS-X and the buoys was less than 15%. Here, all subscenes analysed have a size of 1024 × 1024 pixel. Before analysis, the full TS-X image was rebinned by a factor of 4, i.e. 4 × 4 neighbourhoods of pixels were combined.
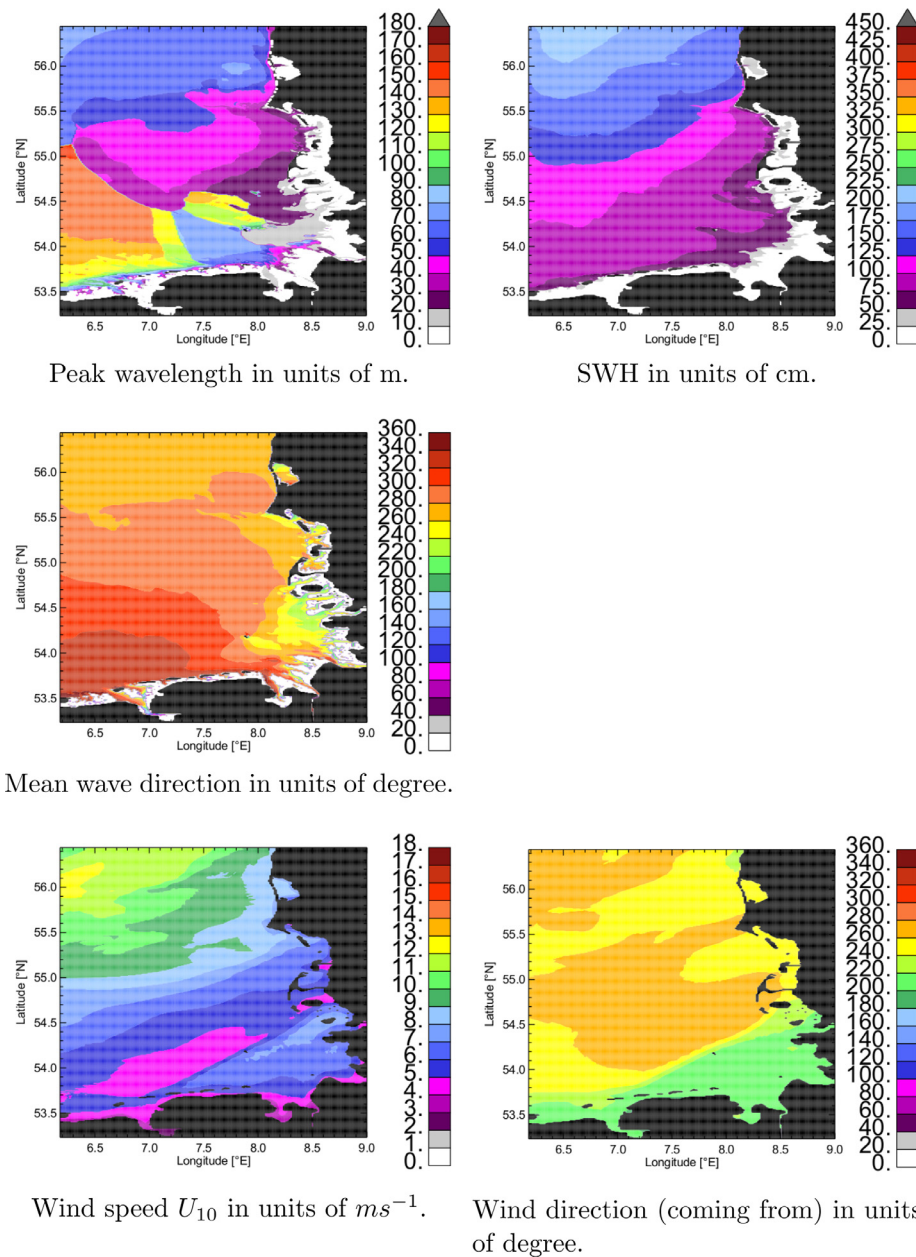
Peak wavelength in units of m.

SWH in units of cm.

Mean wave direction in units of degree.

Wind speed U_{10} in units of ms^{-1}.

Wind direction (coming from) in units of degree.

Fig. 3. CWAM model data on December 3, 2013. The output time is 6 UTC.

Consistent with the pixel spacing of the TS-X images described in Section 2.1.1, the subscene width and length is $1024 \times 4 \times 1.25$ m, i.e. somewhat above 5 km. This subscene size ensures that wavelength differences on the order of few meters are resolvable by the FFT in the wavelength space.

In Fig. 7, a TS-X scene for December 03, 2013 is presented in combination with the resulting peak wavelengths and directions. The latter are given by equidistant arrows overlaid to the scene whose colour is indicative of the value of wavelength (see colour scale on top of Fig. 7). The pattern of arrows arises from the sequence of subscenes analyzed following a raster (i.e. a regular grid with 512 pixel spacing, which is half the subscene size). In Fig. 8, different subscenes and/or their image power spectra are shown. In order to suppress any kind of random spectral noise, a boxcar average was applied to all spectra analyzed in this study. Spectral signals from longer wave-like structures, e.g. wind streaks, were excluded from analysis by high pass filtering.

Subscenes including ships, the breaking of waves, land masses, etc. are a potential source of distortion to their power spectra. Thus, ships were filtered out. A landmask was used to exclude land masses from analysis. This landmask is non-dynamic, i.e. tidal changes between land and sea are not accounted for. For this reason, more filtering was necessary. TS-X data were excluded if the integrated spectral energy exceeded the mean spectral energy of all subscenes not omitted by the landmask by a factor of more than 2.0 (land and breaking waves typically appear relatively bright in radar images and are associated with high spectral energy). In addition, data were excluded if their position was found to be between the mainland and the chain of offshore dune islands (i.e. the East Frisian or North Frisian Islands).

For the comparison between TS-X and CWAM, the month of December 2013 was (arbitrarily) selected. TS-X scenes over the German Bight are available on December 03, 20, 24, and 25 (each having the length of 4–5 single images). The wavelengths resulting from TS-X underwent another pretreatment. Data were omitted from the
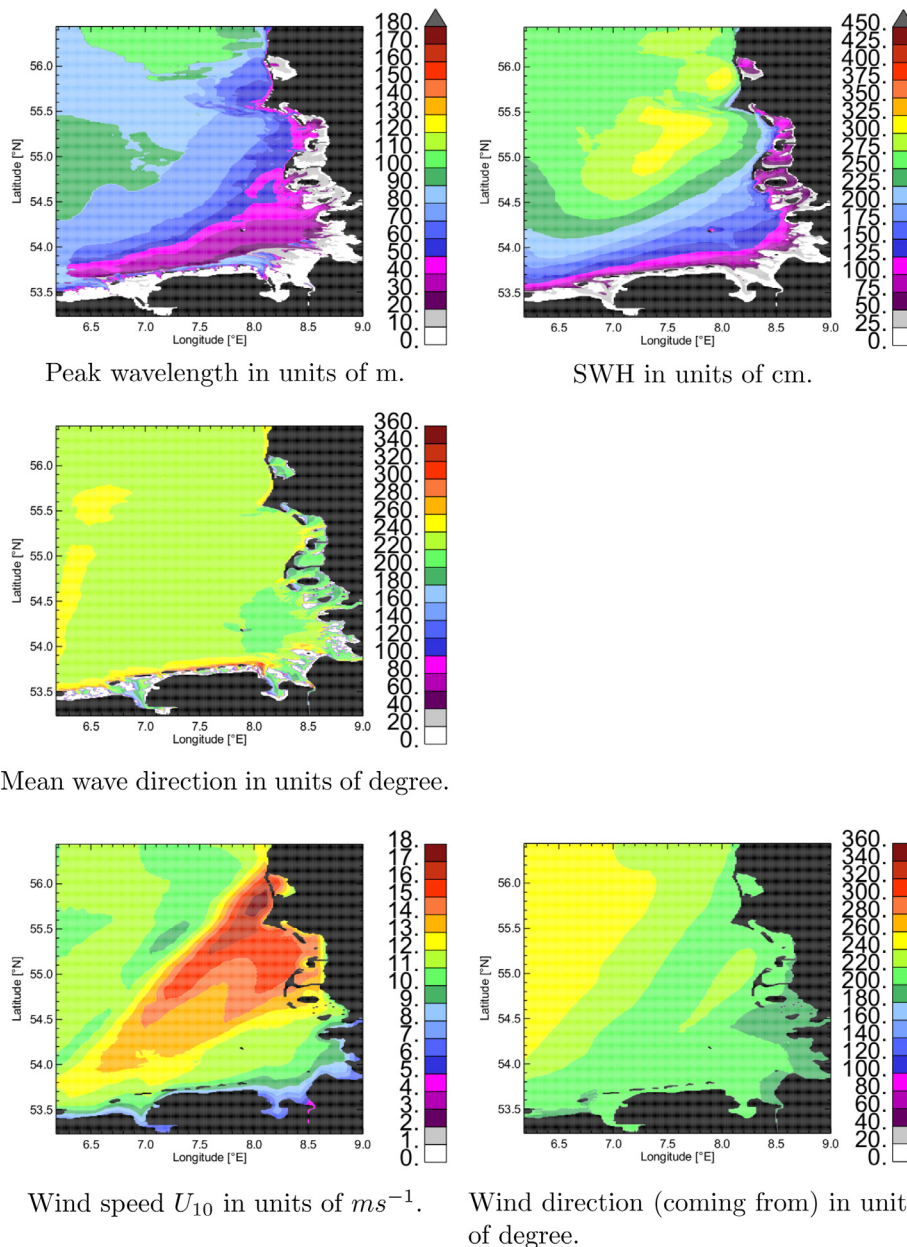
Peak wavelength in units of m.

SWH in units of cm.

Mean wave direction in units of degree.

Wind speed U_{10} in units of ms^{-1}.

Wind direction (coming from) in units of degree.

Fig. 4. CWAM model data on December 20, 2013. The output time is 6 UTC.

comparison if the model value of water depth for the nearest model data point was less than 5 m. A few more pieces of TS-X data affected by the breaking of waves were among the removed data.

2.1.3. Retrieval of the wind speed

The wind speed is inferred from TS-X by the empirical retrieval algorithm XMOD-2. It utilizes radar backscatter coefficients of radar scatterometers for retrieving the wind speed and direction. The radar backscatter, which increases with increasing wind speed and decreasing incidence angle, is dependent on the wind direction to the SAR antenna. This is described by the Geophysical Model Function which was tuned by collocated buoy measurements and model data (Li and Lehner, 2014). In the following, a priori information on the wind direction is taken from the wind input of the CWAM model.

For the wind speed, the data selection criteria of being not flagged by the landmask, not deceeding 1.9 ms^{-1} (this threshold is consistent with Li and Lehner (2014)), and the related CWAM water depth being at least 5 m are used. The number of TS-X/CWAM data pairs per

image is partly somewhat higher for the comparison of wind speed, but generally similar to the comparison of peak wavelength (among others, because only data on the peak wavelength are flagged for high spectral energy as described in Section 2.1.2, not wind data).

2.2. The CWAM model of the DWD

2.2.1. Model data and resolution

The numerical wave model CWAM has a spatial resolution of around ∼900 m. Its forecast is on the order of few days. The intended purpose of CWAM is the operational forecast of meteo-marine parameters on a more refined spatial scale. This information is vital to users like the off-shore industry, coastal authorities, shipping, etc.. Currently, CWAM is run pre-operationally by the DWD (since January 1, 2013). More information can be found at http://www.demarine.de/lr/tp3.

The area of 6.1736°E to 14.9097°E and 53.2292°N to 56.4458°N is covered by CWAM. The spatial coverage is the same for input and

Peak wavelength in units of m.

SWH in units of cm.

Mean wave direction in units of degree.

Wind speed U_{10} in units of ms^{-1}.

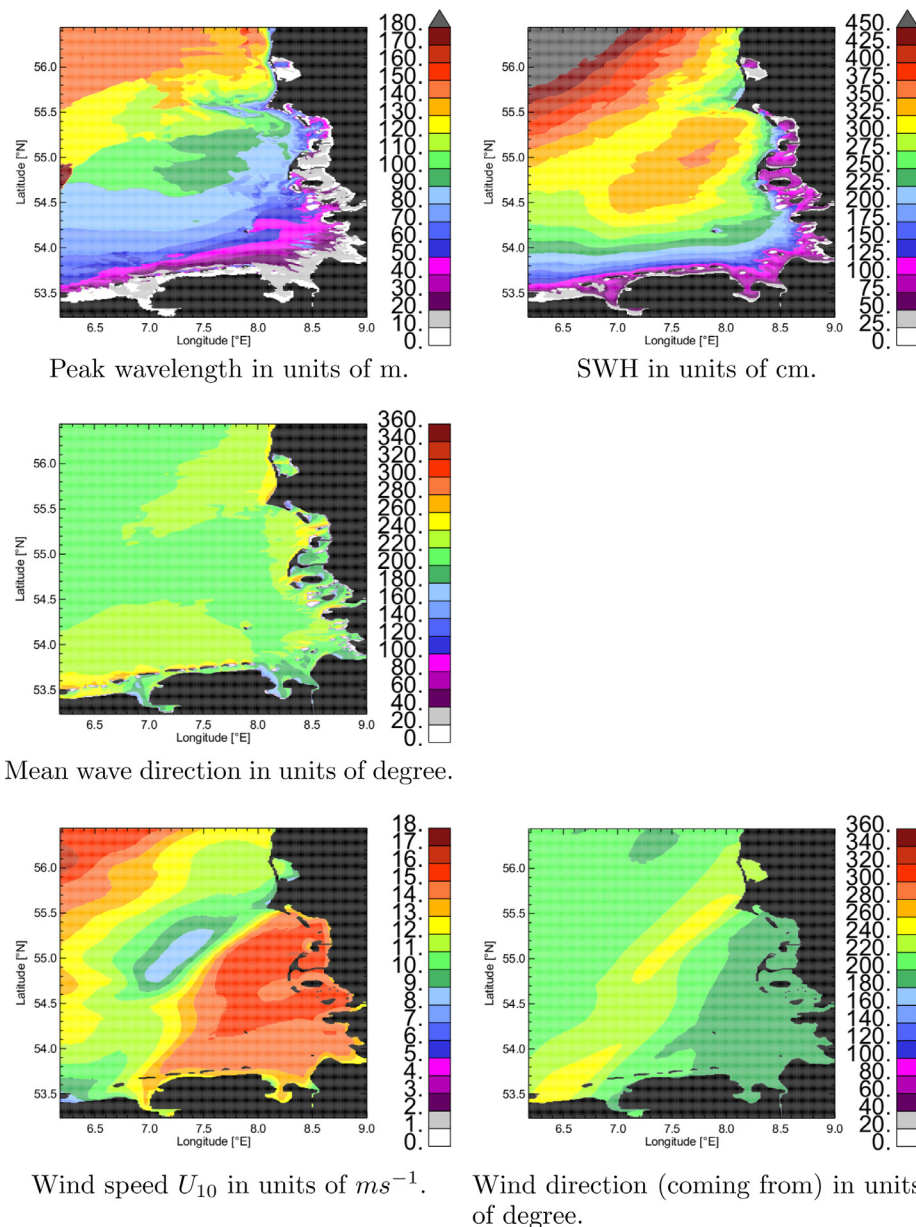Wind direction (coming from) in units of degree.

Fig. 5. CWAM model data on December 24, 2013. The output time is 17 UTC.

output data. An illustration is given in Fig. 1. CWAM is nested within the European Wave Model EWAM of the DWD. Both CWAM and EWAM are based on the third-generation global wave model WAM (=WAve Model; (Hasselmann et al., 1988)). CWAM has 30 × 36 points in the frequency-angle-domain. The time range of the CWAM hindcasts is 12 h at a temporal step of 1 h. Shallow water effects are modelled by applying the Discrete Interaction Approximation (DIA; (Hasselmann et al., 1985)). In addition, bottom friction, depth/current refraction, and wave breaking are accounted for. The CWAM model is driven by winds (10 m above the sea level) from the weather forecast model COSMO-EU, operated by the DWD, as well as water level changes and water currents provided by the ocean model HBM (=Hiromb-Boos-Model), operated by the German Maritime and Hydrographic Agency (Bundesamt für Seeschiffahrt und Hydrographie, BSH). The wind input is updated hourly. Having a spatial resolution of 7 km, the wind is interpolated to the model grid of CWAM. The current/water level input is provided every quarter of an hour and has the same spatial resolution as CWAM.

As already mentioned in the introduction, the quantity compared between TS-X data and CWAM model results is the peak wavelength (not the peak wave direction as CWAM provides the mean wave direction rather than the peak wave direction). The peak wavelength is calculated from different parameters of the model using the linear dispersion relation for water waves. These parameters are the peak period of waves, the water depth, the current speed and direction, and the mean wave direction. An approximation is made by estimating the angle between the peak wave and current direction from the mean wave direction. The calculation is, however, in general not very sensitive to the current-related part of the dispersion relation. Test calculations with the dispersion relation extended for non-linearities, following Li et al. (2003), showed that differences amount to a few meters at most.

2.2.2. Grouping the model data into events

In Figs. 3, 4, 5, and 6, model results on the peak wavelength, mean wave direction, and SWH as well as model input data on the wind speed and direction are shown. These data are provided on four
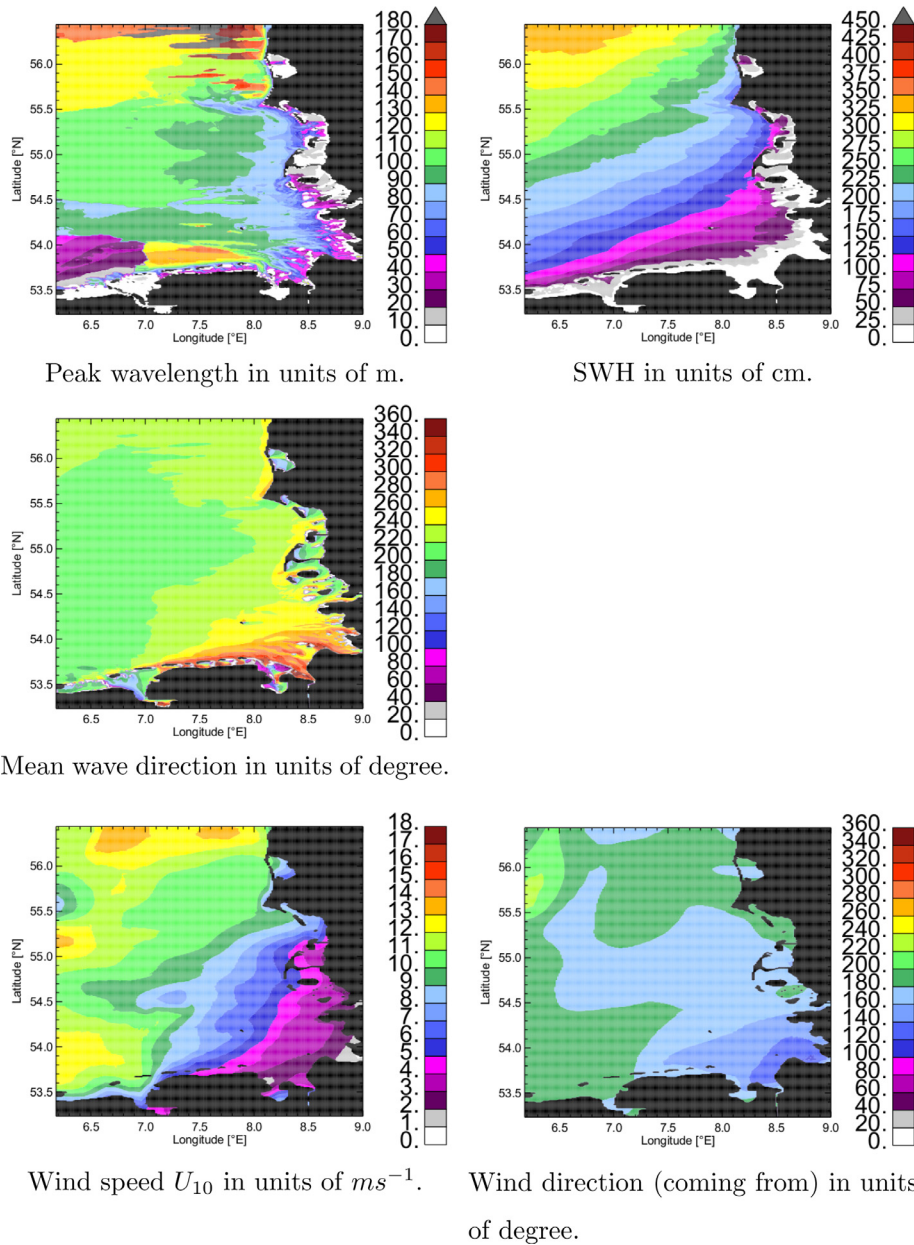
Peak wavelength in units of m.

SWH in units of cm.

Mean wave direction in units of degree.

Wind speed U_{10} in units of ms^{-1}.

Wind direction (coming from) in units of degree.

Fig. 6. CWAM model data on December 25, 2013. The output time is 6 UTC.

different days in December 2013 that are considered further in the following. In this section, the model data for each of these days are coalesced into descriptions of separate events.

Event December 3, 2013, 6 UTC

The wind is coming from SSW (=south-south-west) near to the southern coast and turns clockwise to westerly direction (∼260°) at the northern latitudes. The wind speed is low at ∼5 ms^{-1} in the south and increases to ∼12 ms^{-1} in the northern area.

The mean wave direction follows the wind direction at the northern latitudes. Towards the south, the waves have an increasing component from the north. The SWH decreases in north to south direction as it is expected from the accompanying decrease of water depth. The model output on the peak wavelength indicates that there is at least one wave system of ∼120 m length that is shoaling with the decreasing water depth in the south. In other parts of the area, the spectral peak is located at shorter wavelength.

Event December 20, 2013, 6 UTC

The wind has a southerly direction in the south, turning right into SW (=south-westerly) direction in the NW (=north-western) part of the area. The wind speed increases from ∼12 ms^{-1} in the SW corner to ∼18 ms^{-1} in the NE (=north-eastern) part of the area.

The mean wave direction follows the direction of the wind and comes from SW with a slight turning to the right in the western part. Following the increasing wind speed, the SWH grows up to 3 m into the NE direction. The peak wavelength grows from 30 m at the southern coast towards 80 m in the high wind area. The growth continues towards the north up to 90 m wavelength.

Event December 24, 2013, 17 UTC

This case shows a SW wind direction from the SW corner towards the Danish coast between 55 and 56°N latitude. South and north of that area, the wind has a slightly more southerly direction. The wind speed is between ∼12 and ∼15 ms^{-1} in most of the German Bight. Also north of this area, the wind speed is mainly above ∼10 ms^{-1}.
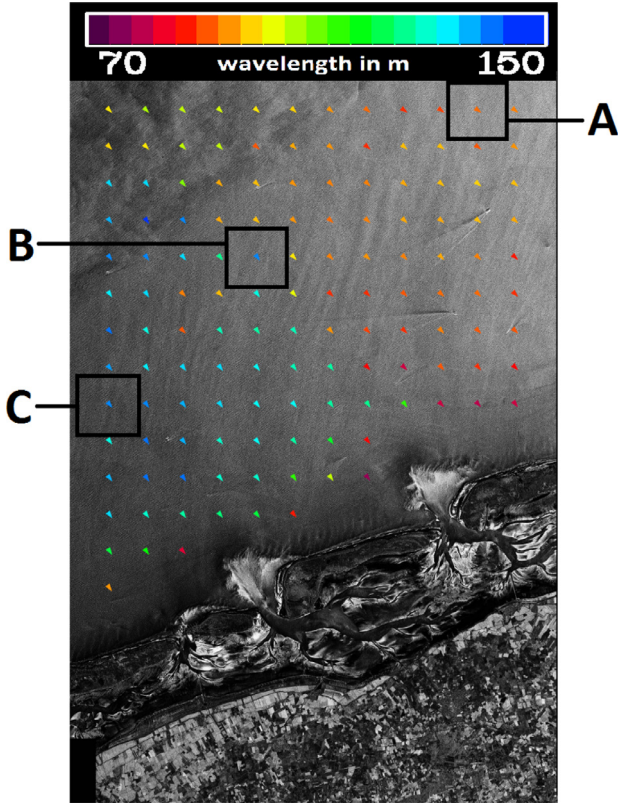
Fig. 7. Stripmap image from TS-X acquired on December 03, 2013 at 5:59:46 UTC over the German North Sea coast (the flight direction of the satellite is from the top to bottom of the image). This image is identical to case A5 in Table 1. The geographical position of the image is provided in Fig. 2, see A5 on December 3. It is tilted by 12.75° with respect to the north south direction. Here, the image is overlaid by coloured arrows indicating the peak wavelength (see colour scale on top of the figure) and also peak wave direction. Three subscenes of the image are highlighted by a black box (label A, B, C). An enlargement of these subscenes and/or their power spectra are shown in Fig. 8.

The mean wave direction follows more the southerly direction of the wind. The SWH and peak wavelength experience an almost perfect orthogonal fetch growth and they grow from the south to the north up to values of ∼4.5 m and ∼140 m, respectively.

Event December 25, 2013, 6 UTC

This event seems to be as well close to an ideal fetch-limited generation case, because the wind blows from SE (=south-east) within the German Bight and changes in the northern and western parts of the area to ∼200°, i.e. from the south with slight components from the west. Since this event happens one day after the previous case, we may remember the wind direction from around 200° to 240° was prevailing throughout the model area in the early evening (∼12 h ago). Here, the wind speed increases from ∼2 ms^{-1} in the inner German Bight to ∼12–13 ms^{-1} in the NW of the area.

The mean wave direction is coming from the south but has a component from the west where the wind has a component from the east. This is caused by the history of the wind field which was blowing from the west in the previous night. The wavelength has some higher values from the previous night near to the southern shore. North of that, the wavelength grows from ∼80 up to ∼130 m.

3. Results

3.1. Statistical parameters used

The results are presented together with their statistical properties such as the bias, root-mean-square difference (RMSE), scatter index

(SI), and correlation. These are calculated from the pairs of all TS-X data for a certain image and their nearest model data points. Let N be the number of such pairs. The bias is determined as the difference between the arithmetic means of model and TS-X data:

$$bias = \left(\frac{\sum_{i=0}^{N} CWAM_i}{N} - \frac{\sum_{i=0}^{N} TSX_i}{N} \right) = \overline{CWAM} - \overline{TSX}, \tag{1}$$

with TSX_i ($CWAM_i$) being the ith piece of TS-X data (CWAM data). The relative bias is calculated as follows:

$$bias_{rel} = \frac{bias}{\overline{TSX}}. \tag{2}$$

The RMSE is given by

$$RMSE = \sqrt{\frac{\sum_{i=0}^{N} (TSX_i - CWAM_i)^2}{N}} \tag{3}$$

and the SI by

$$SI = \frac{RMSE}{\overline{TSX}}. \tag{4}$$

Hence, the bias is a measure for a systematic offset between both datasets while the RMSE and SI are able to take into account the scattering of data. The spatial correlation is calculated as follows:

$$corr = \frac{\frac{1}{N} \sum_{i=0}^{N} ((TSX_i - \overline{TSX})(CWAM_i - \overline{CWAM}))}{\sigma_{TSX}\sigma_{CWAM}}, \tag{5}$$

with σ_{TSX} (σ_{CWAM}) being the standard deviation of the TS-X (CWAM) data. The correlation is a measure how well the spatial patterns of observed and modelled peak wavelength are matching.

3.2. Selected examples

In Fig. 11, the TS-X wavelengths shown before in Fig. 7 are compared to the output from CWAM. The TS-X image, which dates on 5:59:46 UTC, and the model output, for 6 UTC, coincide well in time. The model qualitatively matches the coexistence of two patches of waves observed by TS-X, longer waves in the west and shorter waves in the east. The boundary between longer and shorter waves appears to be shifted slightly westwards by the model. The latter is likely to be the reason of the correlation being not higher than 0.48. With respect to TS-X, the peak wavelengths from CWAM have a negative offset. The bias is around −34 m and the RMSE is around 39 m.

It is worthwhile mentioning that SAR-specific non-linear imaging effects are not necessarily a limitation. Depending on the wave direction, waves down to around ∼20 m length are imaged by TS-X without being cut-off (appendix of Pleskachevsky et al., 2011). Here, reasonable agreement with CWAM was obtained for the TS-X image acquired on December 3, 5:59:17 UTC, with wavelengths being for large parts shorter than 60 m. This comparison is shown in Fig. 12. The bias and RMSE amount for not more than few meters. The correlation is considerably high at a value of 0.85.

In Fig. 13, the peak wavelengths are compared for a TS-X image acquired on December 24, 17:02:24 UTC. Wavelengths between around 60 and 100 m were relatively well predicted by the model. The bias is around 1 m and the RMSE amounts for approximately 10 m. The correlation is 0.66. In this comparison, both the satellite and model show wave shoaling in response to topography. There is a wavelength decrease which clearly follows the shape off Horns Rev. This example demonstrates that the CWAM model is capable of resolving fine-scale features of topography owing to its relatively high spatial resolution.

3.3. All results

All images considered in this study are summarized in Table 1. The images are sorted by time and the latitude and longitude in the image centre are given. In addition, a number from A1 to D5 was given
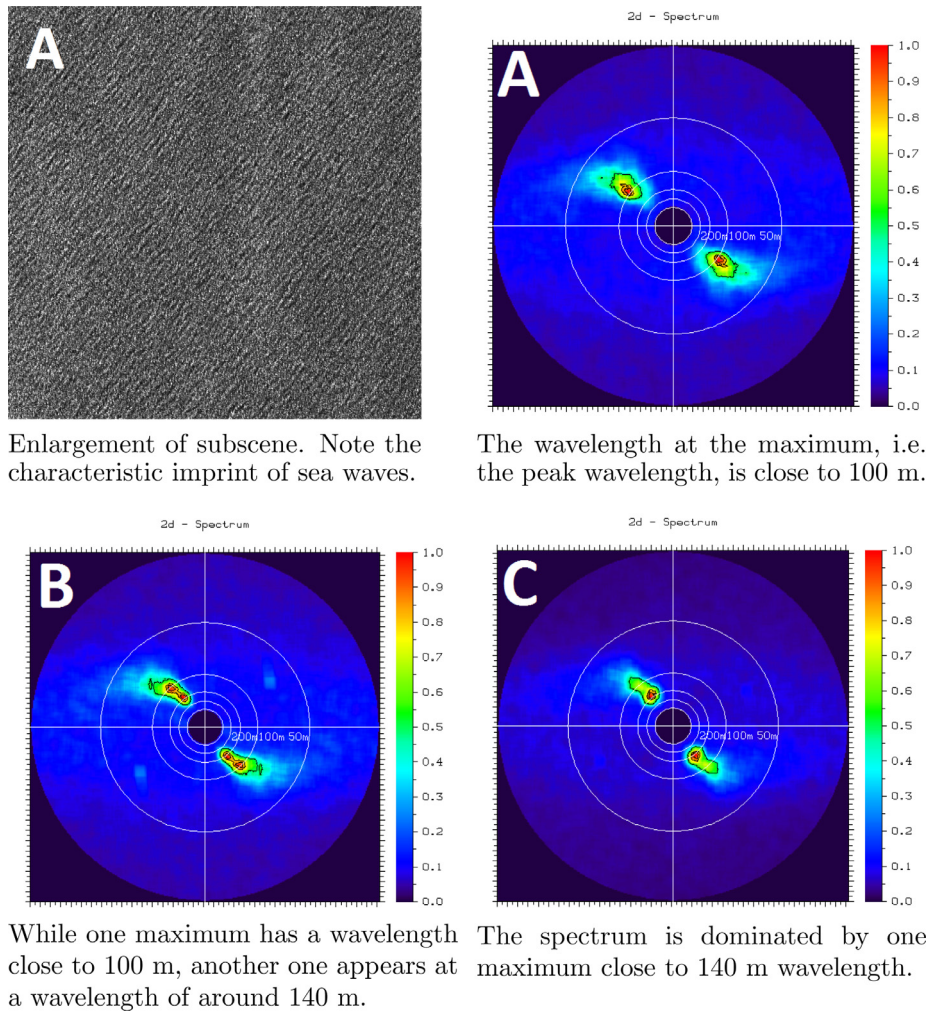
Enlargement of subscene. Note the characteristic imprint of sea waves.

The wavelength at the maximum, i.e. the peak wavelength, is close to 100 m.

While one maximum has a wavelength close to 100 m, another one appears at a wavelength of around 140 m.

The spectrum is dominated by one maximum close to 140 m wavelength.

Fig. 8. Image power spectra related to different subscenes of Fig. 7 (label A, B, C). The spectra are normalized with respect to their maximum value. Due to an ambiguity inherent in Fourier spectra, the spectra have 180° symmetry. High-pass spectral filtering was applied in order to exclude contributions from longer wave-like structures, e.g. wind streaks, from analysis.

to each image. Note that the images were acquired at descending orbit on December 3 (image A1–A5), December 20 (image B1–B4), and December 25 (image D1–D5) and at ascending orbit on December 24 (image C1–C5). Subsequent images with a time step of 7 or 8 s (e.g. A1 and A2) have some overlap. Otherwise, gaps in the wavelength data would arise at their transition due to the subscene size of FFT analysis. A few images which are only 3–5 s apart (e.g. C4 and C5) have around 50% overlap. For each image, the number of data pairs compared between satellite and model is specified. Those images including land have notably less data pairs (e.g. A1). This is a consequence of the landmasking and other data exclusion criteria described in Section 2.1.2. Image C1 has been omitted from wavelength analysis due to its complexity. The latter arises from image features typical in the proximity of land, like sand banks and wind streaks. Separating their signatures from the sea state signals was not possible for a considerable amount of power spectra from this image. For all other images, the results of the wavelength comparison are provided in Table 2.

The results for December 24 (image C1–C5) are governed by the bias and RMSE being relatively low (mostly on the order of 10 m or less) and the correlation being moderate to high. On December 3 and 25 (image A1–A5 and D1–D5), the comparison results require some more differentiated view. Good agreement, such as a bias and RMSE of zero to few meters and correlation of more than 0.8, was obtained for some cases. These are the images A1 and D2. A certain degree of

disagreement resulted for the other images on both days. The results for the images C1–C5, A1, and D2 are proof for the model having the potential to accurately predict the wavelength. By contrast, the bias and RMSE have values of several ten meters throughout December 20 (images B1–B4). The correlation does not exceed 0.64 and is even clearly negative for one of the images.

Besides, the wind input data of CWAM were compared to TS-X results on the wind speed (the TS-X data were retrieved and prepared as described in Section 2.1.3). The results for all images are summarized in Table 3. This is not intended to be a complete validation of the atmospheric model as this is beyond the scope of this article. Comparisons of the SWH between CWAM, TS-X, and buoys including the days of December 3, 20, 24, and 25, 2013 are provided in Pleskachevsky et al. (2015). For most of the measurement buoys included there, data on the peak wave frequency/period are not publicly available (hence, peak wavelengths are not inferred from buoys here).

3.4. Discussion

Obtaining a negative bias between CWAM and TS-X in several cases (e.g. on December 20; images B1–B4) possibly points towards an issue with the peak wave period simulated by the model. Consistent with the linear dispersion relation of water waves, an underestimation of wave period results in an underestimation of wavelength. The peak wave period of CWAM is restricted to a set of discrete
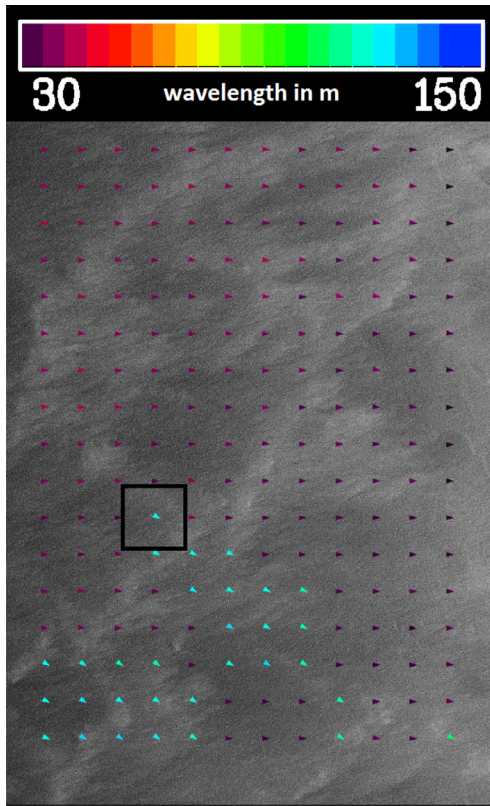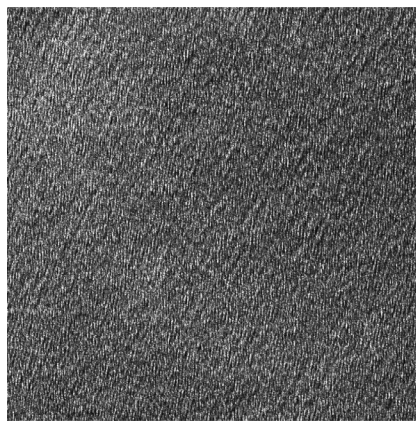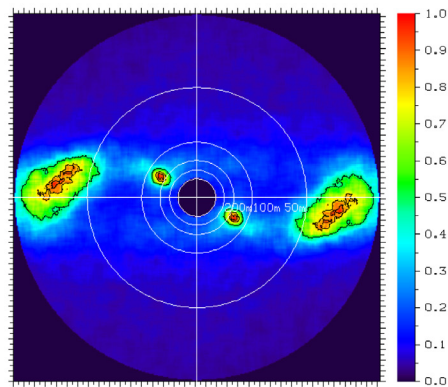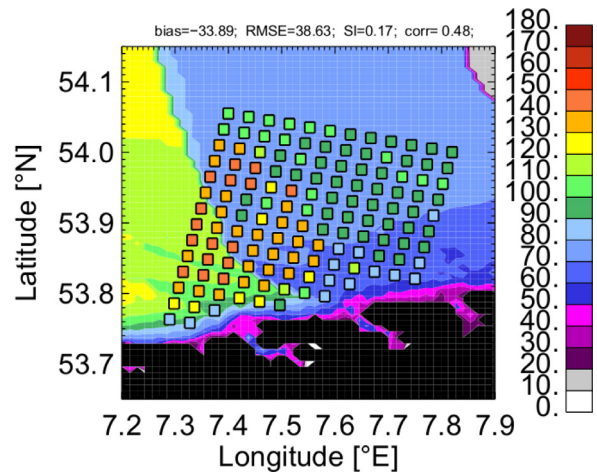
Fig. 11. Comparison of the peak wavelength between TS-X (Stripmap scene acquired on December 03, 2013 at 5:59:46 UTC) and the CWAM model (output for 6 UTC). The TS-X wavelengths are identical to those presented in Fig. 7. The discrete points are the wavelengths from TS-X. The CWAM wavelengths are given by contours. Colour scale on the right (wavelengths in units of m). On top of the Figure, the bias, root mean square difference (RMSE), scatter index (SI), and correlation (corr) are provided. This comparison is identical to case A5 in Table 2.

Fig. 9. Stripmap image from TS-X acquired on December 03, 2013 at 5:59:24 UTC over the German Bight (the flight direction of the satellite is from the top to bottom of the image). This image is identical to case A2 in Table 1. The geographical position of the image is provided in Fig. 2, see A2 on December 3. It is tilted by 12.99° with respect to the north south direction. One subscene of the image is highlighted by a black box. An enlargement of this subscene and its power spectrum are shown in Fig. 10.

values. The intervals between these values are on the order of 1 s. For more details, see the error investigation in Appendix A. As described in Section 3.2, CWAM exhibited a negative bias and a shift in longitude with respect to TS-X data for the image on December 3, 5:59:46 UTC (or A5). As a check, a value of 1 s was added to the CWAM values of peak wave period before being converted to wavelength (for this

conversion, the values of water depth used are tidal corrected). Thus, the agreement between the wavelength from CWAM and TS-X could be considerably improved. The bias and RMSE were approximately halved. The remaining inconsistency was found to be governed by the shift in longitude only. Differently, the bias on December 20 could not be resolved in this simple manner.

Another potential source for disagreement between satellite and model is given by the relative weighting of different spectral peaks of similar strength. These typically arise from an overlay of different regimes of wind sea and swell waves. The satellite data indicate a situation with equally large spectral peaks for image A2 (acquired on December 3, 5:59:24 UTC). The resulting peak wavelengths are shown in Fig. 9. There are short wavelength of 30–45 m length travelling roughly in east to west direction and longer waves of around 120 m length which travel more in the north to south direction. This appears to be a local wind sea and swell waves originating from the Atlantic, respectively. If confining the wavelength comparison to the

Enlargement of subscene. Note that a composite wave pattern consisting of wave regimes of different length is visible.

Different spectral peaks are evident, one at a wavelength of around 40 m and the other at a wavelength between 120 and 130 m.

Fig. 10. Subscene and image power spectrum related to Fig. 9.

Table 1
TS-X satellite images analyzed in this study. The resulting wave and wind parameters are compared to CWAM model data. For each image, a case number, the time of TS-X image acquisition in UTC, the latitude and longitude of the image centre, the CWAM output time in UTC, and the number of data pairs to be compared are specified. The geographical positions of all images are illustrated further in Fig. 2.

TS-X image number	Acquisition time (UTC)	Centre coordinates	CWAM output time (UTC)	Data pairs TS-X/CWAM
A1	Dec. 3, 5:59:17	55.60°N 8.24°E	6:00	55
A2	Dec. 3, 5:59:24	55.16°N 8.06°E	6:00	215
A3	Dec. 3, 5:59:32	54.72°N 7.88°E	6:00	216
A4	Dec. 3, 5:59:39	54.27°N 7.70°E	6:00	212
A5	Dec. 3, 5:59:46	53.82°N 7.53°E	6:00	136
B1	Dec. 20, 5:50:47	55.35°N 8.33°E	6:00	105
B2	Dec. 20, 5:50:54	54.89°N 8.17°E	6:00	158
B3	Dec. 20, 5:51:02	54.43°N 8.01°E	6:00	217
B4	Dec. 20, 5:51:10	53.94°N 7.85°E	6:00	177
C1	Dec. 24, 17:01:57	53.84°N 8.42°E	17:00	–
C2	Dec. 24, 17:02:05	54.34°N 8.24°E	17:00	219
C3	Dec. 24, 17:02:13	54.83°N 8.07°E	17:00	203
C4	Dec. 24, 17:02:21	55.34°N 7.88°E	17:00	218
C5	Dec. 24, 17:02:24	55.55°N 7.80°E	17:00	218
D1	Dec. 25, 5:59:17	55.60°N 8.23°E	6:00	80
D2	Dec. 25, 5:59:24	55.13°N 8.04°E	6:00	240
D3	Dec. 25, 5:59:32	54.63°N 7.84°E	6:00	240
D4	Dec. 25, 5:59:40	54.14°N 7.65°E	6:00	238
D5	Dec. 25, 5:59:45	53.85°N 7.53°E	6:00	146

Table 2
Comparison of the peak wavelength between TS-X and CWAM. For each TS-X image considered in this study, the comparison results are given by the bias in units of m, the root mean square difference (RMSE) in units of m, the scatter index (SI), and the spatial correlation.

Image number	Bias in m	RMSE in m	SI	Correlation
A1	−2.68	5.10	0.11	0.85
A2	−14.12	33.63	0.59	0.08
A3	−87.52	89.76	0.17	0.20
A4	−21.67	36.98	0.26	0.41
A5	−33.89	38.63	0.17	0.48
B1	−25.14	27.61	0.14	0.56
B2	−30.63	31.31	0.07	0.64
B3	−37.09	38.35	0.12	0.19
B4	−48.48	55.34	0.29	−0.44
C1	–	–	–	–
C2	−17.72	19.95	0.13	0.46
C3	−6.32	9.42	0.08	0.68
C4	−6.43	11.71	0.09	0.64
C5	1.08	10.76	0.10	0.66
D1	8.32	20.81	0.23	0.64
D2	0.94	3.15	0.03	0.86
D3	3.12	6.56	0.07	0.54
D4	8.63	19.07	0.19	−0.06
D5	34.12	39.51	0.23	−0.15

Fig. 12. Comparison of the peak wavelength between TS-X (Stripmap scene acquired on December 03, 2013 at 5:59:17 UTC) and the CWAM model (output for 6 UTC). This comparison is identical to case A1 in Table 2. In principle, the same as in Fig. 11.

Fig. 13. Comparison of the peak wavelength between TS-X (Stripmap scene acquired on December 24 at 17:02:24 UTC) and the CWAM model (output for 17 UTC). This comparison is identical to case C5 in Table 2. In principle, the same as in Fig. 11.

short wavelengths only, the agreement between satellite and model improves considerably (183 data pairs compared, bias of −1.45 m, RMSE of 3.72 m, SI of 0.09, correlation of 0.58). As well, this offers an explanation for the discrepancy between satellite and model for image A3 (see Table 2), which follows right south of image A2. The satellite locates the spectral maximum at longer wavelengths of around 120 m length throughout the image. Partly, a secondary spectral maximum is observable at wavelength between 30 and 50 m (note that this wavelength range is already quite close to the cut-off wavelength of TS-X; this is, however, not necessarily a limitation as noted in Section 3.2). By implication, the model seems to give more weight to the latter kind of waves.

The wind input of the model is a factor for data inconsistency as well. Time shifts in the arrival of a wave field may arise from an incorrect wind field provided by the atmospheric model. As mentioned in Section 2.2.1, the CWAM hindcasts are based on wind fields simulated by COSMO-EU that are updated at hourly time steps. Hence, fields of longer waves originating from the passage of an atmospheric front may, in principle, be time-shifted by the model. This has been
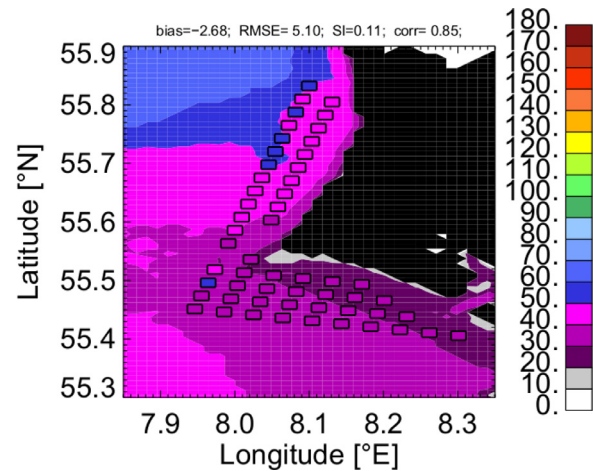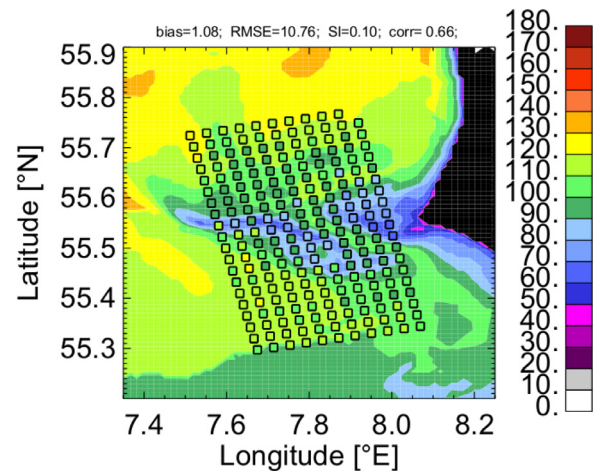
Table 3

Comparison of the wind speed between TS-X data and the CWAM model input. For each TS-X image considered in this study, the comparison results are given by the bias in units of ms^{-1}, the relative bias in %, the mean value of satellite data in units of ms^{-1}, and the mean value of model input in units of ms^{-1}. The mean values were calculated as arithmetic means.

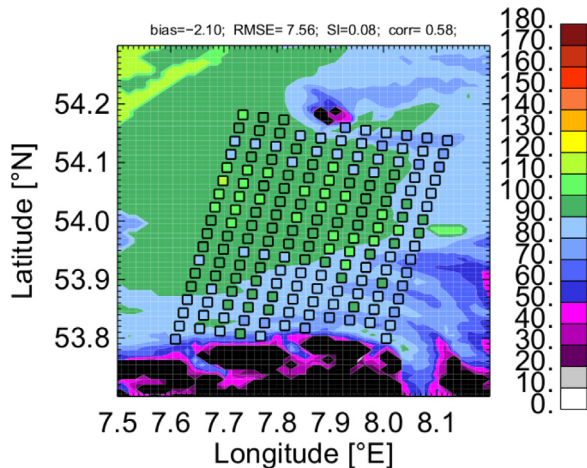| Image number	Bias in ms^{-1}	Relative bias in %	Mean value of satellite data in ms^{-1}	Mean value of model data in ms^{-1}	Data pairs TS-X/CWAM
A1	0.26	3.29	7.96	8.22	66
A2	−0.49	−6.32	7.75	7.26	215
A3	−0.96	−14.27	6.69	5.74	216
A4	−0.88	−15.18	5.79	4.91	212
A5	1.40	30.55	4.58	5.98	135
B1	6.00	64.14	9.35	15.35	107
B2	5.47	57.35	9.54	15.01	159
B3	2.29	22.18	10.31	12.59	217
B4	2.79	32.46	8.60	11.39	177
C1	4.16	40.77	10.20	14.35	148
C2	5.12	52.01	9.84	14.96	219
C3	6.40	71.56	8.94	15.33	203
C4	2.96	31.62	9.36	12.32	217
C5	1.82	20.41	8.90	10.72	218
D1	1.84	23.30	7.89	9.73	81
D2	−0.39	−4.69	8.27	7.88	240
D3	−0.89	−10.98	8.14	7.25	240
D4	0.06	0.89	7.14	7.20	238
D5	2.10	43.51	4.83	6.93	152

Fig. 14. Comparison of the peak wavelength between TS-X (Stripmap image acquired on December 20 at 5:51:10 UTC) and the CWAM model (output for 6 UTC). Here, the peak wavelength from the model were restricted to those waves classified as swell. Without restriction, this comparison would be identical to case B4 in Table 2.

already pointed out to be a source of error with respect to the model results on the SWH in Pleskachevsky et al. (2015). Notable errors may occur when comparing wave data at just one point in time rather than a time series. As a check, the model output one hour earlier and later was compared on December 20 analogously (with and without adding 1 s to the wave model period). This did, however, not significantly improve the results.

Contrastingly, restricting the peak wavelength from the model to those waves classified as swell was able to provide better agreement on December 20, e.g. for image B4. Its geographical position extends from the East Frisian Islands into the sea (shown in Fig. 2, see B4 on December 20). As follows from a detailed view of Fig. 4, upper left panel, the modelled sea state on December 20 consists of a strip of longer waves in close proximity to the islands (blue coloured) and relatively short waves further in the sea (magenta coloured). These are classified as swell waves and wind sea, respectively, by the model. The longer swell waves match those wavelengths obtained from TS-X better than the shorter wind sea waves. The aforementioned restriction is equivalent with forcing all wavelengths

to be swell. Thus, the bias and RMSE are reduced to few meters and the SI and correlation are improved as well (bias of −2.10 m, RMSE of 7.56 m, SI of 0.08, correlation of 0.58; see Fig. 14;). As follows from Table 3, case B1–B4, the wind input of the model on December 20 has the tendency to be overestimated with respect to the wind speed retrieved from TS-X. This suggests the model overemphasizing the interaction between wind and waves. The modelled wind sea component, thus, gaining control over other sea state components is a potential consequence.

4. Summary and outlook

A series of comparisons of the peak wavelength between TS-X satellite images and CWAM model hindcasts was conducted. This involved SAR scenes in the German Bight on four different days in December 2013. Each scene comprises 4–5 Stripmap images of 30×50 km in area. The encountered sea state condition ranged from short to relatively long waves including both systems of wind sea and swell. Reasonable agreement between satellite and model was obtained for large parts. As a result of its high resolution, CWAM was able to match spatial variations in the pattern of the peak wavelength evidenced by TS-X at a relatively high degree of accuracy. These are promising results. Also, comparing modelled data with TS-X seems to be an appropriate validation tool for such high resolution wave forecasts for coastal regions.

Different potential sources of modelling error were discussed. These include an underestimation of the model peak wave period, the relative weighting of different spectral peaks, and the wind input of the model. Test calculations were able to effectively reduce the inconsistency between model and satellite. Among others, it is planned to implement the calculation of an interpolated peak wave period in a future version of CWAM in order to address the issue of the discrete peak wave periods.

Appendix A. The peak of wave energy density for different Fourier space variables

Let $F(k_x, k_y)$ and $E(f, \theta)$ be the spectra of wave energy density in Cartesian wave number coordinates and in frequency direction coordinates. To simplify the computations, we assume that $E(f, \theta)$ can be factorized and written

$$E(f, \theta) = E(f)q(\theta) \tag{A.1}$$

with $q(\theta)$ being independent of frequency and normalized so that the integral over all angles is 1.

With the help of the linear dispersion relation (for simplicity we use the deep water relation)

$$(2\pi f)^2 = gk \tag{A.2}$$

or, after deriving by f,

$$8\pi^2 f = g\frac{dk}{df}, \tag{A.3}$$

we transform the coordinates k_x, k_y and f, θ and their energies into one other:

$$k_x = k\cos(\theta), \quad k_y = k\sin(\theta), \quad \theta = \theta(k_x, k_y),$$
$$f = f(k_x, k_y). \tag{A.4}$$

The same space element has equal energy in both coordinate frames:

$$F(k_x, k_y)dk_x dk_y = E(f, \theta)df d\theta. \tag{A.5}$$

Using the relation between the space elements in Cartesian and polar coordinates,

$$dk_x dk_y = kdkd\theta, \tag{A.6}$$

yields

$$F(k_x, k_y)dk_x dk_y = F(k_x, k_y)kdkd\theta = F(k_x, k_y)k\left(\frac{dk}{df}\right)df d\theta$$
$$= E(f, \theta)df d\theta. \tag{A.7}$$

This implies:

$$E(f, \theta) = F(k_x, k_y)k\frac{dk}{df} = F(k_x, k_y)\frac{2(2\pi)^4 f^3}{g^2}, \tag{A.8}$$

or

$$G(f, \theta) = F(k_x, k_y). \tag{A.9}$$

Consistent with Eq. (A.1), $G(f, \theta)$ has the same directional distribution $q(\theta)$ as $E(f, \theta)$:

$$G(f, \theta) = G(f)q(\theta). \tag{A.10}$$

Inserting this into Eq. (A.8) gives:

$$E(f) = G(f)\frac{2(2\pi)^4 f^3}{g^2}. \tag{A.11}$$

As described in Section 2.2.1, the CWAM model works in frequency and direction space with the coordinates f and θ. Contrastingly, Fourier spectra result from TS-X in wavenumber space with the Cartesian coordinates k_x and k_y. Hence, the spectral peak of $E(f)$ and the peak frequency $f = f_m$ are evidenced by the wave model whereas the peak of $G(f)$ and the peak frequency $f = f_t$ are found by TS-X. f_m and f_t do not completely agree as they are determined by $E'(f_m) = 0$ and $G'(f_t) = 0$. Taylor expansion gives

$$E(f) = E(f_m) + 0.5(f - f_m)^2 E''(f_m) \tag{A.12}$$

in the vicinity of the peak. $E''(f_m)$ is negative because it is the curvature at the maximum. From Eqs. (A.11) and (A.12), the derivative at $f = f_t$ yields

$$(f_t - f_m)E''(f_m) = 2G(f_t)(2\pi)^4 \frac{3f_t^2}{g^2}. \tag{A.13}$$

For the difference of the two peaks we obtain

$$f_t - f_m = \frac{(2G(f_t)(2\pi)^4(\frac{3f_t^2}{g^2}))}{E''(f_m)}$$
$$f_t - f_m = \frac{3}{f_t}\left(\frac{E(f_t)}{E''(f_m)}\right). \tag{A.14}$$

Since $E''(f_m)$ is negative, the model has the tendency to calculate a larger peak frequency or, equivalently, a smaller peak period than TS-X.

References

Beal, R.C., Tilley, D.G., Monaldo, F.M., 1983. Large- and small-scale spatial evolution of digitally processed ocean surface wave spectra from the SEASAT synthetic aperture radar. J. Geophys. Res. 88, 17611778.

Breit, H., Fritz, T., Balss, U., Lachaise, M., Niedermeier, A., Vonavka, M., 2010. TerraSAR-X SAR processing and products. IEEE Trans. Geosci. Remote Sens. 48 (2), 727–740. doi:10.1109/TGRS.2010.2040699.

Bruck, M., Lehner, S., 2012. Sea state measurements using TerraSAR-X data. Proceedings of IGARSS 2012,. IEEE Press. IGARSS 2012, pp. 7609–7612. doi:10.1109/IGARSS.2012.6351866.

Bruck, M., Lehner, S., 2013. Coastal wave field extraction using TerraSAR-X data. J. Appl. Remote Sens. 7 (1). doi:10.1117/1.JRS.7.073694.

Hasselmann, K., Chapron, B., Aouf, L., Ardhuin, F., Collard., F., Engen, G., Hasselmann, S., Heimbach, P., Janssen, P., Johnsen, H., Krogstad, H., Lehner, S., Li, J.-G., Li, X.-M., Rosenthal, W., Schulz-Stellenfleth, J., 2012. The ERS SAR wave mode - a breakthrough in global ocean wave observations. In: ERS Missions: 20 Years of Observing Earth., ESA SP-1326. ESA/ESTEC, Noordwijk, NL, pp. 165–198.

Hasselmann, S., Hasselmann, K., Allender, J.H., Barnett, T.P., 1985. Computations and parameterizations of the non-linear energy transfer in a gravity wave spectrum. Part II: Parameterizations of the non-linear energy transfer for application in wave models. J. Phys. Oceanogr. 15 (11), 13781391.

Hasselmann, S., Hasselmann, K., Janssen, P.A.E.M., Bauer, E., Komen, G.J., Bertotti, L., Lionello, P., Guillaume, A., Cardone, V.C., Greenwood, J.A., 1988. The WAM model - a third generation ocean wave prediction model. J. Phys. Oceanogr. 18, 1775–1810.

Kieser, J., Bruns, T., Lindenthal, A., Brüning, T., Janssen, F., Behrens, A., Li, X.-M., Lehner, S., Pleskachevsky, A., 2013. First studies with the high-resolution coupled wave current model CWAM and other aspects of the project Sea State Monitor. In: Proceedings of the 13th International Workshop on Wave Hindcasting and 4th Coastal Hazard Symposium, Presentation. Banff, Canada. http://www.waveworkshop.org/13thWaves/index.htm. (accessed 27.10.15.).

Lehner, S., Pleskachevsky, A., Velotto, D., Jacobsen, S., 2014. Meteo-marine parameters and their variability observed by high-resolution satellite radar images. Oceanography 26, 8191.

Li, R.J., Yan, Y.X., Cao, H.S., 2003. Nonlinear dispersion relation in wave transformation. China Ocean Eng. 17 (1), 117–122.

Li, X.-M., Lehner, S., 2014. Algorithm for sea surface wind retrieval from TerraSAR-X and TanDEM-X data. IEEE Trans. Geosci. Remote Sens. 52 (5), 2928–2939. doi:10.1109/TGRS.2013.2267780.

Li, X.-M., Lehner, S., Bruns, T., 2011. Ocean wave integral parameter measurements using Envisat ASAR wave mode data. IEEE Trans. Geosci. Remote Sens. 49, 155–174. doi:10.1109/TGRS.2010.2052364.

Li, X.-M., Lehner, S., He, M.-X., 2008. Ocean wave measurements based on satellite synthetic aperture radar (SAR) and numerical wave model (WAM) data - extreme sea state and cross sea analysis. Int. J. Remote Sens. 29, 6403–6416.

Pleskachevsky, A., Gebhardt, C., Rosenthal, W., Lehner, S., Hoffmann, P., Kieser, J., Bruns, T., Lindenthal, A., Jansen, F., Behrens, A., 2015. Satellite-based radar measurements for validation of high-resolution sea state forecast models in the German Bight. Int. Arch. Photogramm. Remote Sens. Spatial Inf. Sci., XL-7/W3 983–990. doi:10.5194/isprsarchives-XL-7-W3-983-2015.

Pleskachevsky, A., Lehner, S., Heege, T., Mott, C., 2011. Synergy and fusion of optical and synthetic aperture radar satellite data for underwater topography estimation in coastal areas. Ocean Dyn. 61 (12). doi:10.1007/s10236-011-0460-1.

Schulz-Stellenfleth, J., König, T., Lehner, S., 2007. An empirical approach for the retrieval of integral ocean wave parameters from synthetic aperture radar data. J. Geophys. Res. 112, C03019. doi:10.1029/2006JC003970.